

Spatial-Angular Interaction for Light Field Image Super-Resolution

Yingqian Wang¹, Longguang Wang¹, Jungang Yang¹, Wei An¹, Jingyi Yu², Yulan Guo^{1,3}

¹College of Electronic Science and Technology, National University of Defense Technology, China

²School of Information Science and Technology, ShanghaiTech University, China

³School of Electronics and Communication Engineering, Sun Yat-sen University, China

{wangyingqian16, wanglongguang15, yangjungang, anwei, yulan.guo}@nudt.edu.cn,

yujingyi@shanghaitech.edu.cn

Abstract

Light field (LF) cameras record both intensity and directions of light rays, and capture scenes from a number of viewpoints. Both information within each perspective (i.e., spatial information) and among different perspectives (i.e., angular information) is beneficial to image super-resolution (SR). In this paper, we propose a spatial-angular interactive network (namely, LF-InterNet) for LF image SR. Specifically, spatial and angular features are first separately extracted from input LFs, and then repetitively interacted to progressively incorporate spatial and angular information. Finally, the interacted features are fused to super-resolve each sub-aperture image. Experiments on 6 public LF datasets demonstrated that our method significantly outperforms the state-of-the-art single image and LF image SR methods both quantitatively and qualitatively.

1. Introduction

Light field (LF) cameras provide multiple views of a scene, and thus enable many attractive applications such as post-capture refocusing [37], depth sensing [26, 17], saliency detection [38, 50], and de-occlusion [36]. However, LF cameras face a trade-off between spatial and angular resolution. That is, they either provide dense angular samplings with low image resolution (e.g., Lytro and RayTrix), or capture high-resolution (HR) sub-aperture images (SAIs) with sparse angular samplings (e.g., camera arrays [41, 28]). Consequently, many efforts have been made to improve the angular resolution through LF reconstruction [43, 42, 19, 12], or the spatial resolution through LF image super-resolution (SR) [1, 51, 23, 34, 45]. In this paper, we focus on the LF image SR problem, namely, to reconstruct HR SAIs from their corresponding low-resolution (LR) SAIs.

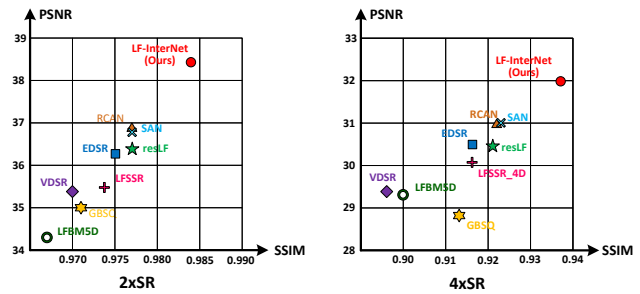


Figure 1. Average PSNR and SSIM values achieved by the state-of-the-art SR methods on 6 public LF datasets [22, 10, 40, 15, 27, 21]. Our LF-InterNet outperforms existing SISR methods (VDSR [13], EDSR [18], RCAN [52], SAN [5]) and LF image SR methods (LFBMSD [1], resLF [51], GBSQ [23], LFSSR [45]) by a large margin in terms of PSNR and SSIM.

Image SR is a long-standing problem in computer vision. To achieve high reconstruction performance, SR methods need to incorporate as much useful information as possible from LR inputs. In the area of single image SR (SISR), good performance can be achieved by fully exploiting the neighborhood context (i.e., spatial information) in an image. Using the spatial information, SISR methods [6, 13, 18, 52, 5, 16, 33] can successfully hallucinate missing details. In contrast, LF cameras capture scenes from multiple views. The complementary information among different views (i.e., angular information) can be used to further improve the performance of LF image SR.

However, due to the complicated 4D structures of LFs, existing LF image SR methods fail to fully exploit both the angular information and the spatial information, resulting in limited SR performance. Specifically, in [48, 47, 49], SAIs are first super-resolved separately using SISR methods [6, 18], and then fine-tuned together to incorporate the angular information. The angular information is ignored by these two-stage methods [48, 47, 49] during their upsam-

pling process. In [34, 51], only part of SAIs are used to super-resolve one view, and the angular information in these discarded views is not incorporated. In contrast, Rossi et al. [23] proposed a graph-based method to consider all angular views in an optimization process. However, this method [23] cannot fully use the spatial information, and is inferior to deep learning-based SR methods [18, 52, 5, 51, 45]. It is worth noting that, even all views are fed to a deep neural network, it is still challenging to achieve superior performance. Yeung et al. [45] proposed a deep neural network named LFSSR to consider all views for LF image SR. However, as shown in Fig. 1, LFSSR is inferior to resLF [51], EDSR [18], RCAN [52], and SAN [5].

The spatial information and angular information are highly coupled in 4D LFs, and contribute to LF image SR in different manners. Consequently, it is difficult for networks to perform well using these coupled information directly. To efficiently incorporate spatial and angular information, we propose a spatial-angular interactive network (i.e., LF-InterNet) for LF image SR. We first re-organize LFs into macro-pixel images (MacPI) and specifically design two convolutions (e.g., spatial/angular feature extractor) to decouple spatial and angular information. Then, we develop LF-InterNet to achieve information interaction between spatial and angular features. Extensive ablation studies have demonstrated the effectiveness and efficiency of our model. Finally, we compare our method to several state-of-the-art single and LF image SR methods on 6 public LF datasets [22, 10, 40, 15, 27, 21]. As shown in Fig. 1, our LF-InterNet outperforms existing SR methods by a large margin in terms of PSNR and SSIM.

2. Related Works

In this section, we briefly review several major works on SISR and LF image SR.

2.1. Single Image SR

In the area of SISR, deep learning-based methods have been extensively explored. Readers are referred to recent surveys [38, 3, 44] for more details in SISR. Here, we only review several milestone works. Dong et al. [6] proposed the first CNN-based SR method (i.e., SRCNN) by cascading 3 convolutional layers. Although SRCNN is shallow and simple, it achieves significant improvements over traditional SR methods. Afterwards, SR networks became increasingly deep and complex, and thus more powerful in spatial information exploitation. Kim et al. [13] proposed a very deep SR network (i.e., VDSR) with 20 convolutional layers. Global residual learning is applied to VDSR to avoid slow convergence. Lim et al. [18] proposed an enhanced deep SR network (i.e., EDSR) and achieved substantial performance improvements by applying both local and global residual learning. Subsequently, Zhang et al. [53] proposed

a residual dense network (i.e., RDN) by combining residual connection and dense connection. RDN can fully extract hierarchical features for image SR, and thus achieve further improvements over EDSR. More recently, Zhang et al. [52] and Dai et al. [5] further improved the performance of SISR by proposing residual channel attention network (i.e., RCAN) and second-order attention network (i.e., SAN). RCAN [52] and SAN [5] are the most powerful methods to date and can achieve a very high reconstruction accuracy.

2.2. LF image SR

In the area of LF image SR, different paradigms have been proposed. Bishop et al. [4] first estimated the scene depth and then used a deconvolution approach to estimate HR SAIs. Wanner et al. [39] proposed a variational LF image SR framework using the estimated disparity map. Farugia et al. [8] decomposed HR-LR patches into several subspaces, and achieved LF image SR via PCA analysis. Alain et al. [1] extended SR-BM3D [7] to LFs, and super-resolved SAIs using LFBM5D filtering. Rossi et al. [23] formulated LF image SR as a graph optimization problem. These traditional methods [4, 39, 8, 1, 23] use different approaches to exploit angular information, but cannot fully exploit spatial information.

In contrast, deep learning-based SR methods are more effective in exploiting spatial information, and thus can achieve promising performance. Many deep learning-based methods have been recently developed for LF image SR. In the pioneering work of LFCNN [48], SAIs are first super-resolved separately using SRCNN [6], and then fine-tuned in pairs to incorporate angular information. Similarly, Yuan et al. [49] proposed LF-DCNN, in which they used EDSR to super-resolve each SAI and then fine-tuned the results. Both LFCNN and LF-DCNN handle the LF image SR problem in two stages, and do not use angular information in the first stage. Different from [48, 49], Wang et al. [34] proposed LFNet by extending BRCN [11] to LF image SR. In their method, SAIs from the same row or column are fed to a recurrent network to incorporate angular information. Zhang et al. [51] stacked SAIs along different angular directions to generate input volumes, and then fed them to a multi-stream residual network named resLF. Both LFNet and resLF reduce 4D LF to 3D LF by using part of SAIs to super-resolve one view. Consequently, angular information in these discarded views cannot be incorporated. To consider all views for LF image SR, Yeung et al. [45] proposed LFSSR to alternately shuffle LF features between SAI pattern and MacPI pattern for convolution. However, the complicated LF structure and coupled information hinders its performance.

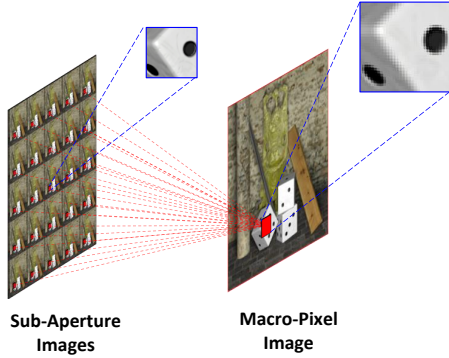


Figure 2. SAI array (left) and MacPI (right) representations of LFs. Both the SAI array and the MacPI representations have the same size of $\mathbb{R}^{UH \times VW}$. Note that, to convert an SAI array representation into a MacPI representation, pixels at the same spatial coordinates of each SAI need to be extracted and organized according to their angular coordinates to generate a macro-pixel. Then, a MacPI can be generated by organizing these macro-pixels according to their spatial coordinates. More details are presented in the supplemental material.

3. Method

3.1. Spatial-Angular Feature Decoupling

A LF has a 4D structure and can be denoted as $\mathcal{L} \in \mathbb{R}^{U \times V \times H \times W}$, where U and V represent the angular dimensions (e.g., $U = 3$, $V = 4$ for a 3×4 LF), H and W represent the height and width of each SAI. Intuitively, a LF can be considered as a 2D angular collection of SAIs, and the SAI at each angular coordinate (u, v) can be denoted as $\mathcal{L}(u, v, :, :) \in \mathbb{R}^{H \times W}$. Similarly, a LF can also be organized into a 2D spatial collection of macro-pixels (namely, a MacPI). The macro-pixel at each spatial coordinate (h, w) can be denoted as $\mathcal{L}(:, :, h, w) \in \mathbb{R}^{U \times V}$. An illustration of these two LF representations is shown in Fig. 2.

Since most methods use SAIs distributed in a square array as their input, we follow [1, 23, 48, 47, 45, 51] to set $U = V = A$ in our method, where A denotes the angular resolution. Given a LF of size $\mathbb{R}^{A \times A \times H \times W}$, both a MacPI and a SAI array can be generated by organizing pixels according to corresponding patterns. Note that, when a LF is organized as a SAI array, the angular information is implicitly contained among different SAIs and thus is hard to extract. Therefore, we use the MacPI representation in our method and design two feature extractors (i.e., Angular Feature Extractor (AFE) and Spatial Feature Extractor (SFE)) to extract and decouple angular and spatial features.

Here, we use a toy example in Fig. 3 to illustrate the process of angular and spatial feature extraction. Specifically, AFE is defined as a convolution with a kernel size of $A \times A$ and a stride of A . Padding is not performed so that features generated by AFE have a size of $\mathbb{R}^{H \times W \times C}$, where C rep-

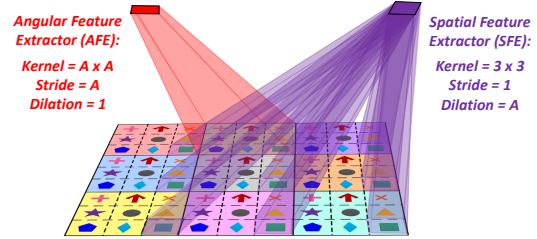


Figure 3. An illustration of angular and spatial feature extractors. Here, a LF of size $\mathbb{R}^{3 \times 3 \times 3 \times 3}$ is used as a toy example. For better visualization, pixels from different SAIs are represented with different labels (e.g., red arrays or green squares), while different macro-pixels are painted with different background colors. Note that, AFE only extracts angular features and SFE only extracts spatial features, resulting in decoupling of spatial-angular information.

resents the feature depth. In contrast, SFE is defined as a convolution with a kernel size of 3×3 , a stride of 1, and a dilation of A . We perform zero padding to ensure that the output features have the same spatial size $AH \times AW$ as the input MacPI. It is worth noting that, during angular feature extraction, each macro-pixel can be exactly convolved by AFE, while the information across different macro-pixels is not aliased. Similarly, during spatial feature extraction, pixels in each SAI can be convolved by SFE, while the angular information is not involved. In this way, the spatial and angular information in a LF is decoupled.

Due to the 3D property of real scenes, objects of different depths have different disparity values in LFs. Consequently, pixels of an object among different views cannot always locate at a single macro-pixel. To address this problem, we apply AFE and SFE for multiple times (i.e., performing spatial-angular interaction) in our network. Consequently, the receptive field can be enlarged to cover pixels with disparities, as shown in Fig. 4.

3.2. Network Design

Our LF-InterNet takes a LR MacPI of size $\mathbb{R}^{AH \times AW}$ as its input and produces a HR SAI array of size $\mathbb{R}^{\alpha AH \times \alpha AW}$, where α denotes the upsampling factor. Following [51, 45], we convert images into YCbCr color space, and only super-resolve the Y channel of images. An overview of our network is shown in Fig. 5.

3.2.1 Overall Architecture

Given a LR MacPI $\mathcal{I}_{LR} \in \mathbb{R}^{AH \times AW}$, the angular and spatial features are first extracted by AFE and SFE, respectively.

$$\mathcal{F}_{A,0} = H_A(\mathcal{I}_{LR}), \quad \mathcal{F}_{S,0} = H_S(\mathcal{I}_{LR}), \quad (1)$$

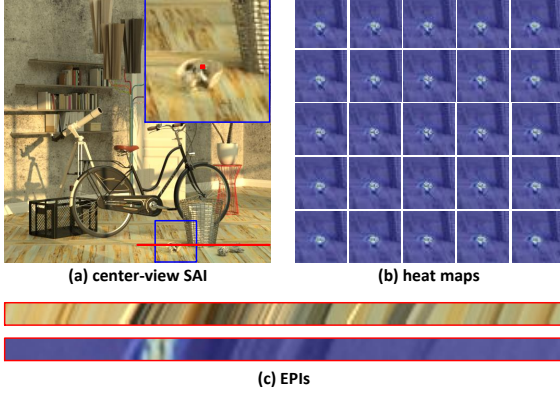


Figure 4. A visualization of the receptive field of our LF-InterNet using the Grad-CAM method [24]. We performed $2\times$ SR on the 5×5 central views of scene *HCnew_bicycle* [10], and investigated the contribution of input pixels to the specified output pixel (marked in the zoom-in image of (a)). (a) Center-view SAI. (b) Heat maps generated by Grad-CAM. The contributive pixels are highlighted. (c) Epipolar-plane images (EPIs) of the output LF and the heat maps. In summary, our LF-InterNet can handle the disparity problem in LF image SR, and its receptive field can cover the corresponding pixels in each LR image.

where $\mathcal{F}_{A,0} \in \mathbb{R}^{H \times W \times C}$ and $\mathcal{F}_{S,0} \in \mathbb{R}^{AH \times AW \times C}$ represent the extracted angular and spatial features, respectively. H_A and H_S represent the angular and spatial feature extractors (as described in Section 3.1), respectively. Once initial features are extracted, features $\mathcal{F}_{A,0}$ and $\mathcal{F}_{S,0}$ are further processed by a set of interaction groups (i.e., Inter-Groups) to achieve spatial-angular feature interaction:

$$(\mathcal{F}_{A,n}, \mathcal{F}_{S,n}) = H_{IG,n}(\mathcal{F}_{A,n-1}, \mathcal{F}_{S,n-1}), \quad (2)$$

$$(n = 1, 2, \dots, N),$$

where $H_{IG,n}$ denotes the n^{th} Inter-Group and N denotes the total number of Inter-Groups.

Inspired by RDN, we cascade all these Inter-Groups to fully use the information interacted at different stages. Specifically, features generated by each Inter-Group are concatenated and fed to a bottleneck block to fuse the interacted information. The feature generated by the bottleneck block is further added with the initial feature $\mathcal{F}_{S,0}$ to achieve global residual learning. The fused feature $\mathcal{F}_{S,t}$ can be obtained by

$$\mathcal{F}_{S,t} = H_B([\mathcal{F}_{A,1}, \dots, \mathcal{F}_{A,N}], [\mathcal{F}_{S,1}, \dots, \mathcal{F}_{S,N}]) + \mathcal{F}_{S,0}, \quad (3)$$

where H_B denotes the bottleneck block, $[\cdot]$ denotes the concatenation operation. Finally, the fused feature $\mathcal{F}_{S,t}$ is fed to the reconstruction module, and a HR SAI array $\mathcal{I}_{SR} \in \mathbb{R}^{\alpha AH \times \alpha AW}$ can be obtained by

$$\mathcal{I}_{SR} = H_{1 \times 1}(S_{pix}(S_{lf}(H_S(\mathcal{F}_{S,t}))))), \quad (4)$$

where S_{lf} , S_{pix} , and $H_{1 \times 1}$ represent LF shuffling, pixel shuffling, and 1×1 convolution, respectively.

3.2.2 Spatial-Angular Feature Interaction

The basic module for spatial-angular interaction is the interaction block (i.e., Inter-Block). As shown in Fig. 5 (b), the Inter-Block takes a pair of angular and spatial features as its inputs to achieve feature interaction. Specifically, the input angular feature is first upsampled by a factor of A . Since pixels in a MacPI can be unevenly distributed due to edges and occlusions in real scenes [20], we learn this discontinuity using a 1×1 convolution and a pixel shuffling layer for angular-to-spatial upsampling. The upsampled angular feature is concatenated with the input spatial feature, and further fed to an SFE to incorporate the spatial and angular information. In this way, the complementary angular information can be used to guide spatial feature extraction. Simultaneously, the new angular feature is extracted from the input spatial feature by an AFE, and then concatenated with the input angular feature. The concatenated angular feature is further fed to a 1×1 convolution to integrate and update the angular information. Note that, the fused angular and spatial features are added with their input features to achieve local residual learning. In this paper, we cascade K Inter-Blocks in an Inter-Group, i.e., the output of an Inter-Block forms the input of its subsequent Inter-Block. In summary, the spatial-angular feature interaction can be formulated as

$$\mathcal{F}_{S,n}^{(k)} = H_S\left([\mathcal{F}_{S,n}^{(k-1)}, (\mathcal{F}_{A,n}^{(k-1)})^\uparrow]\right) + \mathcal{F}_{S,n}^{(k-1)}, \quad (5)$$

$$\mathcal{F}_{A,n}^{(k)} = H_{1 \times 1}\left([\mathcal{F}_{A,n}^{(k-1)}, H_A(\mathcal{F}_{S,n}^{(k-1)})]\right) + \mathcal{F}_{A,n}^{(k-1)}, \quad (6)$$

$$(k = 1, 2, \dots, K),$$

where \uparrow represents the upsampling operation, $\mathcal{F}_{S,n}^{(k)}$ and $\mathcal{F}_{A,n}^{(k)}$ represent the output spatial and angular features of the k^{th} Inter-Block in the n^{th} Inter-Group, respectively.

3.2.3 Feature Fusion and Reconstruction

The objective of this stage is to fuse the interacted features to reconstruct a HR SAI array. The fusion and reconstruction stage mainly consists of bottleneck fusion (as shown in Fig. 5 (c)), LF shuffling (as shown in Fig. 5 (d)), pixel shuffling, and final reconstruction.

In the bottleneck, the concatenated angular features $[\mathcal{F}_{A,1}, \dots, \mathcal{F}_{A,N}] \in \mathbb{R}^{H \times W \times NC}$ are first fed to a 1×1 convolution and a ReLU layer to generate a feature map $\mathcal{F}_A \in \mathbb{R}^{H \times W \times C}$. Then, the squeezed angular feature \mathcal{F}_A is upsampled and concatenated with spatial features. The final fused feature $\mathcal{F}_{S,t}$ can be obtained as

$$\mathcal{F}_{S,t} = H_S([\mathcal{F}_{S,1}, \dots, \mathcal{F}_{S,N}, (\mathcal{F}_A)^\uparrow]) + \mathcal{F}_{S,0}. \quad (7)$$

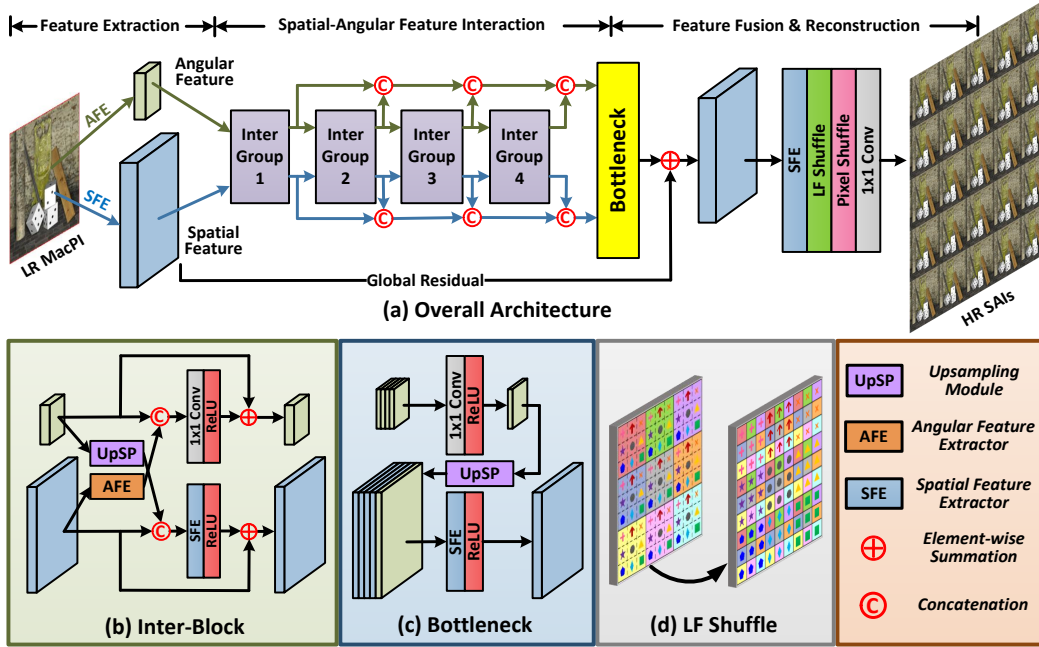


Figure 5. An overview of our LF-InterNet.

After feature fusion, we apply another SFE layer to extend the channel size of $\mathcal{F}_{S,t}$ to $\alpha^2 C$ for pixel shuffling [25]. However, since $\mathcal{F}_{S,t}$ is organized in the MacPI pattern, we apply LF shuffling to convert $\mathcal{F}_{S,t}$ into a SAI array representation for pixel shuffling. To achieve LF shuffling, we first extract pixels with the same angular coordinates in the MacPI feature, and then re-organize these pixels according to their spatial coordinates, which can be formulated as

$$\mathcal{I}_{SAIs}(x, y) = \mathcal{I}_{MacPI}(\xi, \eta), \quad (8)$$

where

$$x = H(\xi - 1) + \lfloor \xi/A \rfloor (1 - AH) + 1, \quad (9)$$

$$y = W(\eta - 1) + \lfloor \eta/A \rfloor (1 - AW) + 1. \quad (10)$$

Here, $x = 1, 2, \dots, AH$ and $y = 1, 2, \dots, AW$ denote the pixel coordinates in the shuffled SAI arrays, ξ and η denote the corresponding coordinates in the input MacPI, $\lfloor \cdot \rfloor$ represents the round-down operation. The derivation of Eqs. (9) and (10) is presented in the supplemental material. Finally, a 1×1 convolution is applied to squeeze the number of feature channels to 1 for HR SAI reconstruction.

4. Experiments

In this section, we first introduce the datasets and our implementation details. Then we conduct ablation studies to investigate our network. Finally, we compare our LF-InterNet to several state-of-the-art LF image SR and SISR methods.

Table 1. Datasets used in our experiments.

Datasets	Type	Training	Test
EPFL [22]	real-world	70	10
HCNew [10]	synthetic	20	4
HCold [40]	synthetic	10	2
INRIA [15]	real-world	35	5
STFgantry [27]	real-world	9	2
STFlytro [21]	real-world	250	50
Total	—	394	73

4.1. Datasets and Implementation Details

As listed in Table 1, we used 6 public LF datasets [22, 10, 40, 15, 27, 21] in our experiments. All the LFs in the training and test sets have an angular resolution of 9×9 . In the training stage, we cropped each SAI into patches of size 64×64 , and then followed the existing SR methods [13, 18, 52, 5, 45, 51] to use bicubic downsampling with a factor of α ($\alpha = 2, 4$) to generate LR patches. The generated LR patches were re-organized into a MacPI pattern to form the input of our network. The L_1 loss function was used since it can generate good results for the SR task and is robust to outliers [2]. Following [51], we augmented the training data by 8 times using random flipping and 90-degree rotation. Note that, during each data augmentation, all SAIs need to be flipped and rotated along both spatial and angular directions to maintain their LF structures.

By default, we used the model with $N = 4$, $K = 4$, $C = 64$, and angular resolution of 5×5 for both $2 \times$ and $4 \times$ SR. We also investigated the performance of other branches of our LF-InterNet in Section 4.2. Following

Table 2. Comparative results achieved on the STFlytro dataset [21] by several variants of our LF-InterNet for $4\times$ SR. Note that, we carefully adjusted the feature depths of different variants to make their model size comparable. FLOPs are computed with an input MacPI of size 160×160 . The results of bicubic interpolation are listed as baselines.

Model	PSNR	SSIM	Params.	FLOPs
Bicubic	27.84	0.855	—	—
LF-InterNet-SpatialOnly	29.98	0.897	5.40M	134.7G
LF-InterNet-AngularOnly	26.57	0.823	5.43M	13.4G
LF-InterNet-SACoupled_1	31.11	0.918	5.42M	5.46G
LF-InterNet-SACoupled_2	31.17	0.919	50.8M	50.5G
LF-InterNet	31.65	0.925	5.23M	50.1G

Table 3. Comparative results achieved on the STFlytro dataset [21] by our LF-InterNet with different number of interactions for $4\times$ SR.

IG_1	IG_2	IG_3	IG_4	PSNR	SSIM
				29.84	0.894
✓				31.44	0.922
✓	✓			31.61	0.924
✓	✓	✓		31.66	0.925
✓	✓	✓	✓	31.84	0.927

[51, 52, 46, 31, 29, 30, 35], we used PSNR and SSIM as quantitative metrics for performance evaluation. Note that, PSNR and SSIM were separately calculated on the Y channel of each SAI. To obtain the overall metric score for a dataset with M scenes (each with an angular resolution of $A\times A$), we first obtain the score for a scene by averaging its A^2 scores, and then obtain the overall score by averaging the scores of all M scenes.

Our LF-InterNet was implemented in PyTorch on a PC with an Nvidia RTX 2080Ti GPU. Our model was initialized using the Xavier method [9] and optimized using the Adam method [14]. The batch size was set to 12 and the learning rate was initially set to 5×10^{-4} and decreased by a factor of 0.5 for every 10 epochs. The training was stopped after 40 epochs and took about one day.

4.2. Ablation Study

In this subsection, we compare the performance of our LF-InterNet with different architectures and angular resolutions to investigate the potential benefits introduced by different design choices.

Angular Information. We investigated the benefit of angular information by removing the angular path in LF-InterNet. That is, we only use SFE for LF image SR. Consequently, the network is identical to a SISR network, and can only incorporate spatial information within each SAI. As shown in Table 2, only using the spatial information, the network (i.e., LF-InterNet-SpatialOnly) achieves a PSNR of 29.98 and a SSIM of 0.897, which are significantly inferior to LF-InterNet. Therefore, the benefit of angular information to LF image SR is clearly demonstrated.

Table 4. Comparisons of different approaches for angular-to-spatial upsampling.

Model	ScI	PSNR/SSIM	ScI	PSNR/SSIM
LF-InterNet-nearest	$2\times$	38.60/0.982	$4\times$	31.65/0.925
LF-InterNet-bilinear	$2\times$	37.67/0.976	$4\times$	30.71/0.911
LF-InterNet	$2\times$	38.81/0.983	$4\times$	31.84/0.927

Table 5. Comparative results achieved on the STFlytro dataset [21] by our LF-InterNet with different angular resolutions for $2\times$ and $4\times$ SR.

AngRes	Scall	PSNR	SSIM	Scale	PSNR	SSIM
3×3	$2\times$	37.95	0.980	$4\times$	31.30	0.918
5×5	$2\times$	38.81	0.983	$4\times$	31.84	0.927
7×7	$2\times$	39.05	0.984	$4\times$	32.04	0.931
9×9	$2\times$	39.08	0.985	$4\times$	32.07	0.933

Spatial Information. To investigate the benefit introduced by spatial information, we changed the kernel size of all SFEs from 3×3 to 1×1 . In this case, the spatial information cannot be exploited and integrated by convolutions. As shown in Table 2, the performance of LF-InterNet-AngularOnly is even inferior to bicubic interpolation. That is because, neighborhood context in an image is highly significant in recovering details. It is clear that spatial information plays a major role in LF image SR, while angular information can only be used as a complementary part to spatial information but cannot be used alone.

Information Decoupling. To investigate the benefit of spatial-angular information decoupling, we stacked all SAIs along the channel dimension as input, and used 3×3 convolutions with a stride of 1 to extract both spatial and angular information from these stacked images. Note that, the cascaded framework with global and local residual learning was maintained to keep the overall network architecture unchanged. To achieve fair comparison, we adjusted the feature depths to keep the model size (i.e., LF-InterNet-SACoupled_1) or computational complexity (i.e., LF-InterNet-SACoupled_2) comparable to LF-InterNet. As shown in Table 2, both LF-InterNet-SACoupled_1 and LF-InterNet-SACoupled_2 are inferior to LF-InterNet. It is clearly demonstrated that, our LF-InterNet can handle the 4D LF structure and achieve LF image SR much more efficiently by using the proposed spatial-angular feature decoupling mechanism.

Spatial-Angular Interaction. We investigated the benefits introduced by our spatial-angular interaction mechanism. Specifically, we canceled feature interaction in each Inter-Group by removing upsampling and AFE modules in each Inter-Block (see Fig. 5 (b)). In this case, spatial and angular features can only be processed separately. When all interactions are removed, these spatial and angular features can only be incorporated by the bottleneck block. Table 3 presents the results achieved by our LF-InterNet with different numbers of interactions. It can be observed that, without any feature interaction, our network achieves a very

Table 6. PSNR/SSIM values achieved by different methods for $2\times$ and $4\times$ SR.

Method	Scale	Dataset						
		EPLF [22]	HCNew [10]	HCold [40]	INRIA [15]	STFgantry [27]	STFlytro [21]	Average
Bicubic	$2\times$	29.50/0.935	31.69/0.934	37.46/0.978	31.10/0.956	30.82/0.947	33.02/0.950	32.27/0.950
VDSR [13]	$2\times$	32.01/0.959	34.37/0.956	40.34/0.985	33.80/0.972	35.80/0.980	35.91/0.970	35.37/0.970
EDSR [18]	$2\times$	32.86/0.965	35.02/0.961	41.11/0.988	34.61/0.977	37.08/0.985	36.87/0.975	36.26/0.975
RCAN [52]	$2\times$	33.46/0.967	35.56/0.963	41.59/0.989	35.18/0.978	38.18/0.988	37.32/0.977	36.88/0.977
SAN [5]	$2\times$	33.36/0.967	35.51/0.963	41.47/0.989	35.15/0.978	37.98/0.987	37.26/0.976	36.79/0.977
LFBM5D [1]	$2\times$	31.15/0.955	33.72/0.955	39.62/0.985	32.85/0.969	33.55/0.972	35.01/0.966	34.32/0.967
GBSQ [23]	$2\times$	31.22/0.959	35.25/0.969	40.21/0.988	32.76/0.972	35.44/0.983	35.04/0.956	34.99/0.971
LFSSR [45]	$2\times$	32.56/0.967	34.47/0.960	41.04/0.989	34.06/0.976	34.08/0.975	36.62/0.976	35.47/0.974
resLF [51]	$2\times$	33.22/0.969	35.79/0.969	42.30/0.991	34.86/0.979	36.28/0.985	35.80/0.970	36.38/0.977
LF-InterNet	$2\times$	34.76/0.976	37.20/0.976	44.65/0.995	36.64/0.984	38.48/0.991	38.81/0.983	38.42/0.984
Bicubic	$4\times$	25.14/0.831	27.61/0.851	32.42/0.934	26.82/0.886	25.93/0.843	27.84/0.855	27.63/0.867
VDSR [13]	$4\times$	26.82/0.869	29.12/0.876	34.01/0.943	28.87/0.914	28.31/0.893	29.17/0.880	29.38/0.896
EDSR [18]	$4\times$	27.82/0.892	29.94/0.893	35.53/0.957	29.86/0.931	29.43/0.921	30.29/0.903	30.48/0.916
RCAN [52]	$4\times$	28.31/0.899	30.25/0.896	35.89/0.959	30.36/0.936	30.25/0.934	30.66/0.909	30.95/0.922
SAN [5]	$4\times$	28.30/0.899	30.25/0.898	35.88/0.960	30.29/0.936	30.30/0.933	30.71/0.909	30.96/0.923
SRGAN [16]	$4\times$	26.85/0.870	28.95/0.873	34.03/0.942	28.85/0.916	28.19/0.898	29.28/0.883	29.36/0.897
ESRGAN [33]	$4\times$	25.59/0.836	26.96/0.819	33.53/0.933	27.54/0.880	28.00/0.905	27.09/0.826	28.12/0.867
LFBM5D [1]	$4\times$	26.61/0.869	29.13/0.882	34.23/0.951	28.49/0.914	28.30/0.900	29.07/0.881	29.31/0.900
GBSQ [23]	$4\times$	26.02/0.863	28.92/0.884	33.74/0.950	27.73/0.909	28.11/0.901	28.37/0.873	28.82/0.913
LFSSR [45]	$4\times$	27.39/0.894	29.61/0.893	35.40/0.962	29.26/0.930	28.53/0.908	30.26/0.908	30.08/0.916
resLF [51]	$4\times$	27.86/0.899	30.37/0.907	36.12/0.966	29.72/0.936	29.64/0.927	28.94/0.891	30.44/0.921
LF-InterNet	$4\times$	29.52/0.917	31.01/0.917	37.23/0.972	31.65/0.950	30.44/0.941	31.84/0.927	31.95/0.937

low reconstruction accuracy (i.e., 29.84 in PSNR and 0.894 in SSIM). That is because, the angular and spatial information cannot be effectively incorporated by the bottleneck block without feature interactions. As the number of interactions increases, the performance is steadily improved. This clearly demonstrates the effectiveness of our spatial-angular feature interaction mechanism.

Angular-to-Spatial Upsampling. To demonstrate the effectiveness of the pixel shuffling layer used in angular-to-spatial upsampling, we introduced two variants by replacing pixel shuffling with nearest upsampling and bilinear upsampling, respectively. It can be observed from Table 4 that LF-InterNet-bilinear achieves much lower PSNR and SSIM scores than LF-InterNet-nearest and LF-InterNet. That is because, bilinear interpolation introduces aliasing among macro-pixels during angular-to-spatial upsampling, resulting in ambiguities in spatial-angular feature decoupling and interaction. In contrast, both nearest upsampling and pixel shuffling do not introduce aliasing and thus achieve improved performance. Moreover, since pixels in a macro-pixel can be unevenly distributed due to edges and occlusions in real scenes [20], pixel shuffling achieves a further improvement over nearest upsampling due to its discontinuity modeling within macro-pixels.

Angular Resolution. In this section, we analyze the performance of LF-InterNet with different angular resolutions. Specifically, we extracted the central SAIs with size of $A \times A$ ($A = 3, 5, 7, 9$) from the input LFs, and trained different models for both $2\times$ and $4\times$ SR. As shown in Table 5, the PSNR and SSIM values for both $2\times$ and $4\times$ SR

are improved as the angular resolution is increased. That is because, additional views provide rich angular information for LF image SR. It is also notable that, the improvement tends to be saturated when the angular resolution is further increased from 7×7 to 9×9 (with only 0.03 dB improvement in PSNR). That is because, the complementary information provided by additional views is already sufficient. Since the angular information has been fully exploited for an angular resolution of 7×7 , a further increase of views can only provide minor performance improvement.

4.3. Comparison to the State-of-the-arts

We compare our method to several state-of-the-art methods including 6 SISR methods [13, 18, 52, 5, 16, 33] and 4 LF image SR methods [1, 23, 45, 51]. All these methods were implemented using their released codes and pre-trained models. We also present the results of bicubic interpolation as the baseline results. For simplicity, we only present the results on 5×5 LFs for $2\times$ and $4\times$ SR. Since the angular resolution of LFSSR is fixed, we use its original version with 8×8 input SAIs.

Quantitative Results. Quantitative results are presented in Table 6. For both $2\times/4\times$ SR, our LF-InterNet achieves the best results on all the 6 datasets and outperforms existing methods by a large margin. Specifically, for $2\times$ and $4\times$ SR, an improvement of 2.04 and 1.51 dB in PSNR is achieved over the state-of-the-art LF image SR method resLF [51], while an improvement of 1.54 and 1.00 dB in PSNR is achieved over the state-of-the-art SISR method RCAN [52].

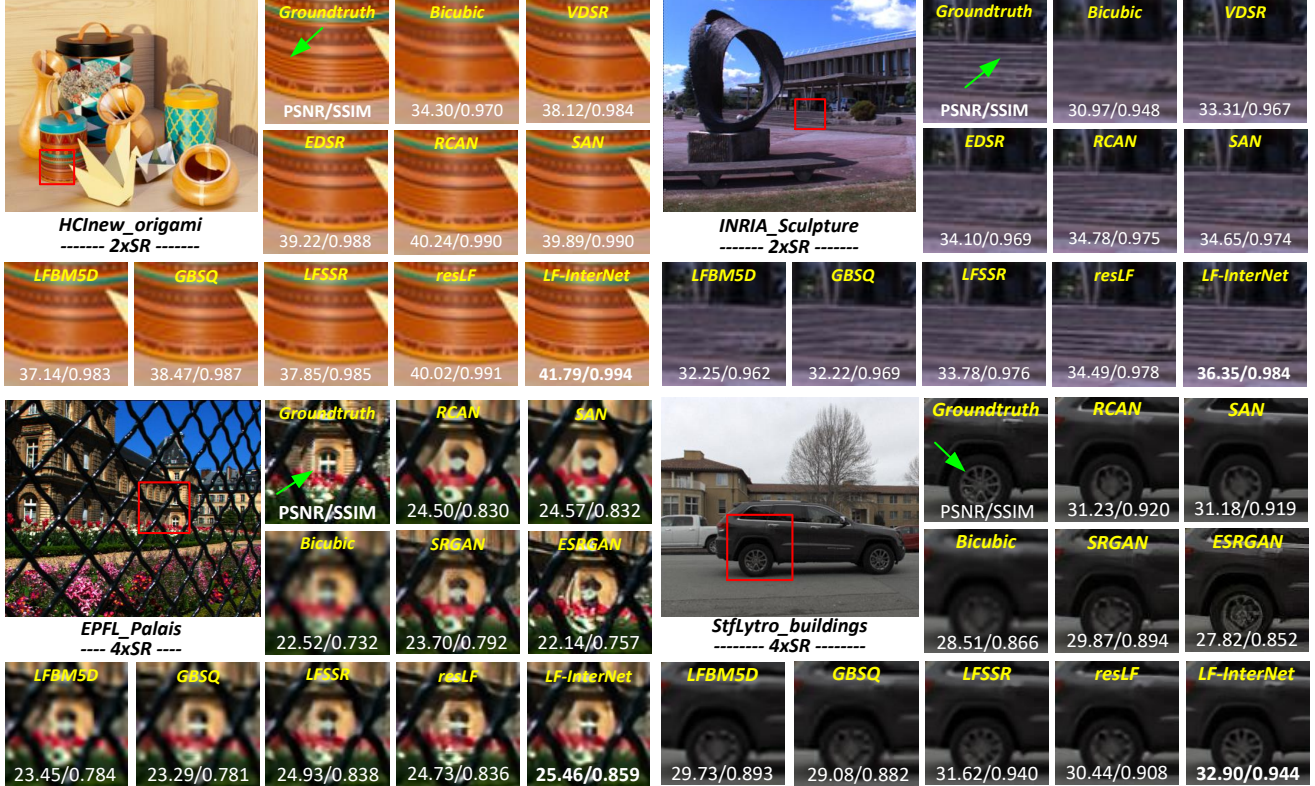


Figure 6. Visual results of $2\times$ and $4\times$ SR.

Table 7. Comparisons of model size and memory consumption for $2\times$ and $4\times$ SR. Note that, the memory consumption is calculated on an input LF with a size of $5\times 5\times 32\times 32$. The PSNR/SSIM scores are averaged over the 6 datasets [22, 10, 40, 15, 27, 21].

Method	Scale	Params.	FLOPs	PSNR / SSIM	Scale	Params.	FLOPs	PSNR / SSIM
RCAN [52]	$2\times$	15.44M	392.87G	36.88 / 0.977	$4\times$	15.59M	408.53G	30.95 / 0.922
SAN [5]	$2\times$	15.71M	401.16G	36.79 / 0.977	$4\times$	15.86M	416.82G	31.96 / 0.923
resLF [51]	$2\times$	6.35M	37.06G	36.38 / 0.977	$4\times$	6.79M	39.70G	30.08 / 0.916
LF-InterNet ₃₂	$2\times$	1.20M	11.87G	37.88 / 0.983	$4\times$	1.31M	12.53G	31.57 / 0.933
LF-InterNet ₆₄	$2\times$	4.80M	47.46G	38.42 / 0.984	$4\times$	5.23M	50.10G	31.95 / 0.937

Qualitative Results. Qualitative results of $2\times$ and $4\times$ SR are shown in Fig. 6, with more visual comparisons being provided in our supplemental material. Our LF-InterNet can well preserve the textures and details (e.g., the horizontal stripes in the scene *HCInew_origami* and the stairway in the scene *INRIA_Sculpture*) in the super-resolved images. In contrast, state-of-the-art SISR methods RCAN [52] and SAN [5] produce oversmoothed images with poor details. The visual superiority of our method is more obvious for $4\times$ SR. That is because, the input LR images are severely degraded by the down-sampling operation, and the process of $4\times$ SR is highly ill-posed. In such cases, some perceptual-oriented methods (e.g., SRGAN [16] and ESRGAN [33]) use spatial information only to hallucinate missing details, resulting in ambiguous and even fake textures (e.g., the window frame in scene *EPFL_Palais* and the wheel in scene *StfLytro_buildings*). In contrast, our method can use complementary angular information among

different views to produce more faithful results, and achieve the highest PSNR/SSIM scores.

Efficiency. We further compare our LF-InterNet to RCAN [52], SAN [5], and resLF [51] in terms of model sizes (i.e., the number of parameters) and memory consumption (i.e., FLOPs). As shown in Table 7, our LF-InterNet achieves superior SR performance with less parameters and lower FLOPs. Note that, although the feature depth of our model is halved to 32, our method (i.e., LF-InterNet₃₂) can still achieve higher PSNR/SSIM scores than RCAN, SAN, and resLF. The model sizes of LF-InterNet₃₂ are 1.20M for $2\times$ SR and 1.31M for $4\times$ SR, while its memory consumption is 11.87G for $2\times$ SR and 12.53G for $4\times$ SR. This clearly demonstrates the high efficiency of our network architecture.

Performance w.r.t. Perspectives. Since our LF-InterNet can super-resolve all SAIs in a LF, we further investigate the reconstruction quality with respect to different

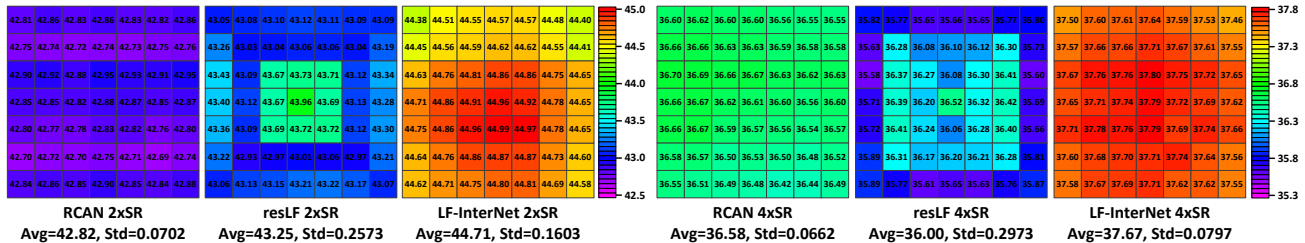


Figure 7. PSNR values achieved by RCAN [52], resLF [51] and LF-InterNet on each perspective of scene *HCIold_MonasRoom* [40]. Here, 7×7 input views are used to perform both $2 \times$ and $4 \times$ SR. We use standard deviation (Std) of PSNR scores among views to represent their uniformity. Our LF-InterNet achieves high reconstruction quality and balanced distribution among different SAIs.

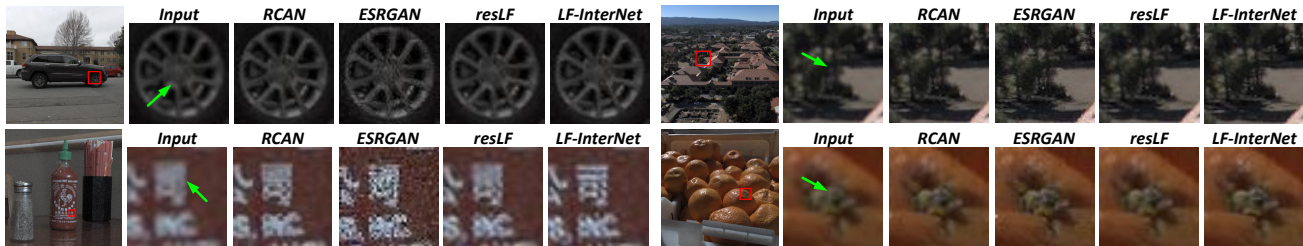


Figure 8. Visual results achieved by different methods under real-world degradation.

Table 8. Comparative results achieved on the UCSD dataset for $2 \times$ and $4 \times$ SR.

Method	Scale	PSNR/SSIM	Scale	PSNR/SSIM
RCAN [52]	$2 \times$	41.63 / 0.983	$4 \times$	36.49 / 0.955
SAN [5]	$2 \times$	41.56 / 0.983	$4 \times$	36.57 / 0.956
resLF [51]	$2 \times$	41.29 / 0.982	$4 \times$	35.89 / 0.953
LF-InterNet	$2 \times$	42.36 / 0.985	$4 \times$	37.12 / 0.960

perspectives. We used the central 7×7 views of scene *HCIold_MonasRoom* to perform both $2 \times$ and $4 \times$ SR. The PSNR values are calculated for each perspective and are visualized in Fig. 7. Since resLF uses part of views to super-resolve different perspectives, the reconstruction qualities of resLF for non-central views are relatively low. In contrast, our LF-InterNet jointly uses the angular information from all input views to super-resolve each perspective, and thus achieves higher reconstruction quality (i.e., higher PSNR values) and a more balanced distribution (i.e., lower Std scores) among different perspectives.

Generalization to Unseen Scenarios. We evaluate the generalization capability of different methods by testing them on a novel and unseen real-world dataset (i.e., the UCSD dataset [32]). Note that, all methods have not been trained or fine-tuned on the UCSD dataset. Results in Table 8 show that our LF-InterNet outperforms RCAN [52], SAN [5], and resLF [51], which clearly demonstrate the generalization capability of our method to unseen scenarios.

Performance Under Real-World Degradation. We compare the performance of different methods under real-world degradation by directly applying them to LFs in the STFlytro dataset [21]. As shown in Fig. 8, our method pro-

duces images with faithful details and less artifacts. Since the LF structure keeps unchanged under both bicubic and real-world degradation, our method can learn to incorporate spatial and angular information from training LFs using the proposed spatial-angular interaction mechanism. It is also demonstrated that our method can be easily applied to LF cameras to generate high-quality images.

5. Conclusion

In this paper, we proposed a deep convolutional network LF-InterNet for LF image SR. We first introduce an approach to extract and decouple spatial and angular features, and then design a feature interaction mechanism to incorporate spatial and angular information. Experimental results have clearly demonstrated the superiority of our method. Our LF-InterNet outperforms the state-of-the-art SR methods by a large margin in terms of PSNR and SSIM, and can recover faithful details in the reconstructed images.

6. Acknowledgement

This work was partially supported by the National Natural Science Foundation of China (No. 61972435, 61602499), Natural Science Foundation of Guangdong Province, Fundamental Research Funds for the Central Universities (No. 18lgzd06).

References

- [1] Martin Alain and Aljosa Smolic. Light field super-resolution via lfbm5d sparse coding. In *2018 25th IEEE International*

- Conference on Image Processing (ICIP)*, pages 2501–2505. IEEE, 2018.
- [2] Yildiray Anagun, Sahin Isik, and Erol Seke. Srlibrary: Comparing different loss functions for super-resolution over various convolutional architectures. *Journal of Visual Communication and Image Representation*, 61:178–187, 2019.
- [3] Saeed Anwar, Salman Khan, and Nick Barnes. A deep journey into super-resolution: A survey. *arXiv preprint arXiv:1904.07523*, 2019.
- [4] Tom E Bishop and Paolo Favaro. The light field camera: Extended depth of field, aliasing, and superresolution. *IEEE Transactions on Pattern Analysis and Machine Intelligence*, 34(5):972–986, 2011.
- [5] Tao Dai, Jianrui Cai, Yongbing Zhang, Shu-Tao Xia, and Lei Zhang. Second-order attention network for single image super-resolution. In *Proceedings of the IEEE Conference on Computer Vision and Pattern Recognition*, pages 11065–11074, 2019.
- [6] Chao Dong, Chen Change Loy, Kaiming He, and Xiaoou Tang. Learning a deep convolutional network for image super-resolution. In *European Conference on Computer Vision (ECCV)*, pages 184–199. Springer, 2014.
- [7] Karen Egiazarian and Vladimir Katkovnik. Single image super-resolution via bm3d sparse coding. In *European Signal Processing Conference (EUSIPCO)*, pages 2849–2853. IEEE, 2015.
- [8] Reuben A Farrugia, Christian Galea, and Christine Guillemot. Super resolution of light field images using linear subspace projection of patch-volumes. *IEEE Journal of Selected Topics in Signal Processing*, 11(7):1058–1071, 2017.
- [9] Xavier Glorot and Yoshua Bengio. Understanding the difficulty of training deep feedforward neural networks. In *Proceedings of the International Conference on Artificial Intelligence and Statistics*, pages 249–256, 2010.
- [10] Katrin Honauer, Ole Johannsen, Daniel Kondermann, and Bastian Goldluecke. A dataset and evaluation methodology for depth estimation on 4d light fields. In *Asian Conference on Computer Vision (ACCV)*, pages 19–34. Springer, 2016.
- [11] Yan Huang, Wei Wang, and Liang Wang. Bidirectional recurrent convolutional networks for multi-frame super-resolution. In *Advances in Neural Information Processing Systems (NeurIPS)*, pages 235–243, 2015.
- [12] Jing Jin, Junhui Hou, Hui Yuan, and Sam Kwong. Learning light field angular super-resolution via a geometry-aware network. *AAAI, arXiv preprint arXiv:2002.11263*, 2020.
- [13] Jiwon Kim, Jung Kwon Lee, and Kyoung Mu Lee. Accurate image super-resolution using very deep convolutional networks. In *Proceedings of the IEEE Conference on Computer Vision and Pattern Recognition (CVPR)*, pages 1646–1654, 2016.
- [14] Diederik P Kingma and Jimmy Ba. Adam: A method for stochastic optimization. *Proceedings of the International Conference on Learning and Representation (ICLR)*, 2015.
- [15] Mikael Le Pendu, Xiaoran Jiang, and Christine Guillemot. Light field inpainting propagation via low rank matrix completion. *IEEE Transactions on Image Processing*, 27(4):1981–1993, 2018.
- [16] Christian Ledig, Lucas Theis, Ferenc Huszár, Jose Caballero, Andrew Cunningham, Alejandro Acosta, Andrew Aitken, Alykhan Tejani, Johannes Totz, Zehan Wang, et al. Photo-realistic single image super-resolution using a generative adversarial network. In *Proceedings of the IEEE conference on computer vision and pattern recognition*, pages 4681–4690, 2017.
- [17] Titus Leistner, Hendrik Schilling, Radek Mackowiak, Stefan Gumhold, and Carsten Rother. Learning to think outside the box: Wide-baseline light field depth estimation with epishift. In *2019 International Conference on 3D Vision (3DV)*, pages 249–257. IEEE, 2019.
- [18] Bee Lim, Sanghyun Son, Heewon Kim, Seungjun Nah, and Kyoung Mu Lee. Enhanced deep residual networks for single image super-resolution. In *Proceedings of the IEEE Conference on Computer Vision and Pattern Recognition Workshops (CVPRW)*, pages 136–144, 2017.
- [19] Nan Meng, Hayden Kwok-Hay So, Xing Sun, and Edmund Lam. High-dimensional dense residual convolutional neural network for light field reconstruction. *IEEE Transactions on Pattern Analysis and Machine Intelligence*, 2019.
- [20] In Kyu Park, Kyoung Mu Lee, et al. Robust light field depth estimation using occlusion-noise aware data costs. *IEEE transactions on pattern analysis and machine intelligence*, 40(10):2484–2497, 2017.
- [21] Abhilash Sunder Raj, Michael Lowney, Raj Shah, and Gordon Wetzstein. Stanford lytro light field archive, 2016.
- [22] Martin Rerabek and Touradj Ebrahimi. New light field image dataset. In *International Conference on Quality of Multimedia Experience (QoMEX)*, 2016.
- [23] Mattia Rossi and Pascal Frossard. Geometry-consistent light field super-resolution via graph-based regularization. *IEEE Transactions on Image Processing*, 27(9):4207–4218, 2018.
- [24] Ramprasaath R Selvaraju, Michael Cogswell, Abhishek Das, Ramakrishna Vedantam, Devi Parikh, and Dhruv Batra. Grad-cam: Visual explanations from deep networks via gradient-based localization. In *Proceedings of the IEEE International Conference on Computer Vision (ICCV)*, pages 618–626, 2017.
- [25] Wenzhe Shi, Jose Caballero, Ferenc Huszár, Johannes Totz, Andrew P Aitken, Rob Bishop, Daniel Rueckert, and Zehan Wang. Real-time single image and video super-resolution using an efficient sub-pixel convolutional neural network. In *Proceedings of the IEEE Conference on Computer Vision and Pattern Recognition (CVPR)*, pages 1874–1883, 2016.
- [26] Changha Shin, Hae-Gon Jeon, Youngjin Yoon, In So Kweon, and Seon Joo Kim. Epinet: A fully-convolutional neural network using epipolar geometry for depth from light field images. In *Proceedings of the IEEE Conference on Computer Vision and Pattern Recognition*, pages 4748–4757, 2018.
- [27] Vaibhav Vaish and Andrew Adams. The (new) stanford light field archive. *Computer Graphics Laboratory, Stanford University*, 6(7), 2008.
- [28] Kartik Venkataraman, Dan Lelescu, Jacques Duparré, Andrew McMahon, Gabriel Molina, Priyam Chatterjee, Robert Mullis, and Shree Nayar. Picam: An ultra-thin high performance monolithic camera array. *ACM Transactions on Graphics*, 32(6):166, 2013.

- [29] Longguang Wang, Yulan Guo, Zaiping Lin, Xinpu Deng, and Wei An. Learning for video super-resolution through hr optical flow estimation. In *Asian Conference on Computer Vision*, pages 514–529. Springer, 2018.
- [30] Longguang Wang, Yulan Guo, Li Liu, Zaiping Lin, Xinpu Deng, and Wei An. Deep video super-resolution using hr optical flow estimation. *IEEE transactions on Image Processing*, 2020.
- [31] Longguang Wang, Yingqian Wang, Zhengfa Liang, Zaiping Lin, Jungang Yang, Wei An, and Yulan Guo. Learning parallax attention for stereo image super-resolution. In *Proceedings of the IEEE Conference on Computer Vision and Pattern Recognition*, pages 12250–12259, 2019.
- [32] Ting-Chun Wang, Jun-Yan Zhu, Ebi Hiroaki, Manmohan Chandraker, Alexei A Efros, and Ravi Ramamoorthi. A 4d light-field dataset and cnn architectures for material recognition. In *European Conference on Computer Vision*, pages 121–138. Springer, 2016.
- [33] Xintao Wang, Ke Yu, Shixiang Wu, Jinjin Gu, Yihao Liu, Chao Dong, Yu Qiao, and Chen Change Loy. Esrgan: Enhanced super-resolution generative adversarial networks. In *Proceedings of the European Conference on Computer Vision (ECCV)*, pages 0–0, 2018.
- [34] Yunlong Wang, Fei Liu, Kunbo Zhang, Guangqi Hou, Zhenan Sun, and Tieniu Tan. Lfnet: A novel bidirectional recurrent convolutional neural network for light-field image super-resolution. *IEEE Transactions on Image Processing*, 27(9):4274–4286, 2018.
- [35] Yingqian Wang, Longguang Wang, Jungang Yang, Wei An, and Yulan Guo. Flickr1024: A large-scale dataset for stereo image super-resolution. In *Proceedings of the IEEE International Conference on Computer Vision Workshops*, pages 0–0, 2019.
- [36] Yingqian Wang, Tianhao Wu, Jungang Yang, Longguang Wang, Wei An, and Yulan Guo. Deocnet: Learning to see through foreground occlusions in light fields. In *Winter Conference on Applications of Computer Vision (WACV)*. IEEE, 2020.
- [37] Yingqian Wang, Jungang Yang, Yulan Guo, Chao Xiao, and Wei An. Selective light field refocusing for camera arrays using bokeh rendering and superresolution. *IEEE Signal Processing Letters*, 26(1):204–208, 2018.
- [38] Zhihao Wang, Jian Chen, and Steven CH Hoi. Deep learning for image super-resolution: A survey. *arXiv preprint arXiv:1902.06068*, 2019.
- [39] Sven Wanner and Bastian Goldluecke. Variational light field analysis for disparity estimation and super-resolution. *IEEE Transactions on Pattern Analysis and Machine Intelligence*, 36(3):606–619, 2013.
- [40] Sven Wanner, Stephan Meister, and Bastian Goldluecke. Datasets and benchmarks for densely sampled 4d light fields. In *Vision, Modelling and Visualization (VMV)*, volume 13, pages 225–226. Citeseer, 2013.
- [41] Bennett Wilburn, Neel Joshi, Vaibhav Vaish, Eino-Ville Talvala, Emilio Antunez, Adam Barth, Andrew Adams, Mark Horowitz, and Marc Levoy. High performance imaging using large camera arrays. In *ACM Transactions on Graphics*, volume 24, pages 765–776. ACM, 2005.
- [42] Gaochang Wu, Yebin Liu, Qionghai Dai, and Tianyou Chai. Learning sheared epi structure for light field reconstruction. *IEEE Transactions on Image Processing*, 28(7):3261–3273, 2019.
- [43] Gaochang Wu, Mandan Zhao, Liangyong Wang, Qionghai Dai, Tianyou Chai, and Yebin Liu. Light field reconstruction using deep convolutional network on epi. In *Proceedings of the IEEE Conference on Computer Vision and Pattern Recognition (CVPR)*, pages 6319–6327, 2017.
- [44] Wenming Yang, Xuechen Zhang, Yapeng Tian, Wei Wang, Jing-Hao Xue, and Qingmin Liao. Deep learning for single image super-resolution: A brief review. *IEEE Transactions on Multimedia*, 2019.
- [45] Henry Wing Fung Yeung, Junhui Hou, Xiaoming Chen, Jie Chen, Zhibo Chen, and Yuk Ying Chung. Light field spatial super-resolution using deep efficient spatial-angular separable convolution. *IEEE Transactions on Image Processing*, 28(5):2319–2330, 2018.
- [46] Xinyi Ying, Yingqian Wang, Longguang Wang, Weidong Sheng, Wei An, and Yulan Guo. A stereo attention module for stereo image super-resolution. *IEEE Signal Processing Letters*, 2020.
- [47] Youngjin Yoon, Hae-Gon Jeon, Donggeun Yoo, Joon-Young Lee, and In So Kweon. Light-field image super-resolution using convolutional neural network. *IEEE Signal Processing Letters*, 24(6):848–852, 2017.
- [48] Youngjin Yoon, Hae-Gon Jeon, Donggeun Yoo, Joon-Young Lee, and In So Kweon. Learning a deep convolutional network for light-field image super-resolution. In *Proceedings of the IEEE International Conference on Computer Vision Workshops (ICCVW)*, pages 24–32, 2015.
- [49] Yan Yuan, Ziqi Cao, and Lijuan Su. Light-field image super-resolution using a combined deep cnn based on epi. *IEEE Signal Processing Letters*, 25(9):1359–1363, 2018.
- [50] Miao Zhang, Jingjing Li, JI WEI, Yongri Piao, and Huchuan Lu. Memory-oriented decoder for light field salient object detection. In *Advances in Neural Information Processing Systems*, pages 896–906, 2019.
- [51] Shuo Zhang, Youfang Lin, and Hao Sheng. Residual networks for light field image super-resolution. In *Proceedings of the IEEE Conference on Computer Vision and Pattern Recognition (CVPR)*, pages 11046–11055, 2019.
- [52] Yulun Zhang, Kunpeng Li, Kai Li, Lichen Wang, Bineng Zhong, and Yun Fu. Image super-resolution using very deep residual channel attention networks. In *Proceedings of the European Conference on Computer Vision (ECCV)*, pages 286–301, 2018.
- [53] Yulun Zhang, Yapeng Tian, Yu Kong, Bineng Zhong, and Yun Fu. Residual dense network for image super-resolution. In *Proceedings of the IEEE Conference on Computer Vision and Pattern Recognition (CVPR)*, pages 2472–2481, 2018.

Spatial-Angular Interaction for Light Field Image Super-Resolution

Supplemental Material

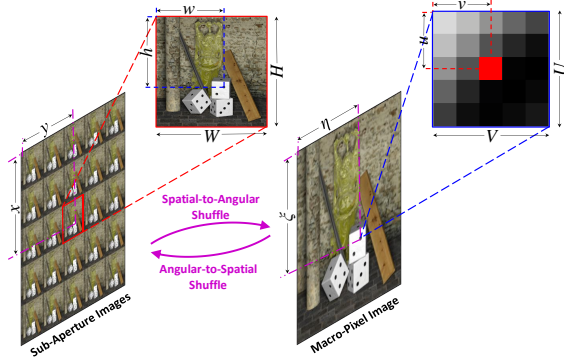


Figure 9. An illustration of the LF shuffling operation. Since the SAIs and the MacPI denote the same LF, the objective of LF shuffling is to re-organize LFs between these two representations.

Section **A** presents details of the light field (LF) shuffling operation. Section **B** provides additional visual comparisons for $2\times$ and $4\times$ SR.

A. Light Field Shuffle

We use the notations in Table 9 for formulation. As shown in Fig. 9, a LF $\mathcal{L} \in \mathbb{R}^{U \times V \times H \times W}$ can be organized into a macro-pixel image (MacPI) $\mathcal{I}_{MacPI} \in \mathbb{R}^{UH \times VW}$ or an array of sub-aperture images (SAIs) $\mathcal{I}_{SAIs} \in \mathbb{R}^{UH \times VW}$. Consequently, LF shuffling is defined as the transformation between these two representations. To convert LFs from one representation to the other representation, the one-to-one mapping function between MacPI and SAIs needs to be built. Without loss of generality, we take spatial-to-angular shuffling as an example, namely, to find point $(\xi, \eta) \in \mathcal{I}_{MacPI}$ corresponding to a known point $(x, y) \in \mathcal{I}_{SAIs}$. We first calculate the angular coordinates u and v of point (x, y) according to

$$u = \lceil x/H \rceil = \lfloor x/H \rfloor + 1, \quad (11)$$

$$v = \lceil y/W \rceil = \lfloor y/W \rfloor + 1. \quad (12)$$

Using the angular coordinates, the spatial coordinates h and w can be derived by

$$h = x - (u - 1) \cdot H = x - \lfloor x/H \rfloor \cdot H, \quad (13)$$

$$w = y - (v - 1) \cdot W = y - \lfloor y/W \rfloor \cdot W. \quad (14)$$

Table 9. Notations used in this supplemental material.

Notation	Representation
$\mathcal{L} \in \mathbb{R}^{U \times V \times H \times W}$	a 4D LF
$\mathcal{I}_{SAIs} \in \mathbb{R}^{UH \times VW}$	a 2D SAI array
$\mathcal{I}_{MacPI} \in \mathbb{R}^{UH \times VW}$	a 2D MacPI
$U, V \in \mathbb{Z}_+$	angular size
$H, W \in \mathbb{Z}_+$	spatial size
$u, v \in \mathbb{Z}_+$	angular coordinate
$h, w \in \mathbb{Z}_+$	spatial coordinate
$(x, y) \in \mathbb{Z}_+^2$	coordinate in \mathcal{I}_{SAIs}
$(\xi, \eta) \in \mathbb{Z}_+^2$	coordinate in \mathcal{I}_{MacPI}
$\lfloor \cdot \rfloor$	round-down operation

Since \mathcal{I}_{SAIs} and \mathcal{I}_{MacPI} represent the same LF, (x, y) and (ξ, η) in these two representations have the same spatial and angular coordinates. Therefore, we find (ξ, η) corresponding to (u, v, h, w) as follows:

$$\begin{aligned} \xi &= U \cdot (h - 1) + u \\ &= U \cdot (x - \lfloor x/H \rfloor \cdot H - 1) + \lfloor x/H \rfloor + 1 \\ &= U \cdot (x - 1) + \lfloor x/H \rfloor \cdot (1 - U \cdot H) + 1 \end{aligned} \quad (15)$$

$$\begin{aligned} \eta &= V \cdot (w - 1) + v \\ &= V \cdot (y - \lfloor y/W \rfloor \cdot W - 1) + \lfloor y/W \rfloor + 1 \\ &= V \cdot (y - 1) + \lfloor y/W \rfloor \cdot (1 - V \cdot W) + 1 \end{aligned} \quad (16)$$

The angular-to-spatial shuffle can be derived following a similar approach:

$$\begin{aligned} x &= H \cdot (u - 1) + h \\ &= H \cdot (\xi - 1) + \lfloor \xi/U \rfloor \cdot (1 - U \cdot H) + 1 \end{aligned} \quad (17)$$

$$\begin{aligned} y &= W \cdot (v - 1) + w \\ &= W \cdot (\eta - 1) + \lfloor \eta/V \rfloor \cdot (1 - V \cdot W) + 1 \end{aligned} \quad (18)$$

Note that, Eqs. (9-10) in the main body of our manuscript can be derived from the above equations (i.e., Eqs. (7-8)) by assigning A to U and V .

B. Additional Visual Comparisons

Additional visual comparisons for $2\times$ and $4\times$ SR are shown in Figs. 10 and 11, respectively.

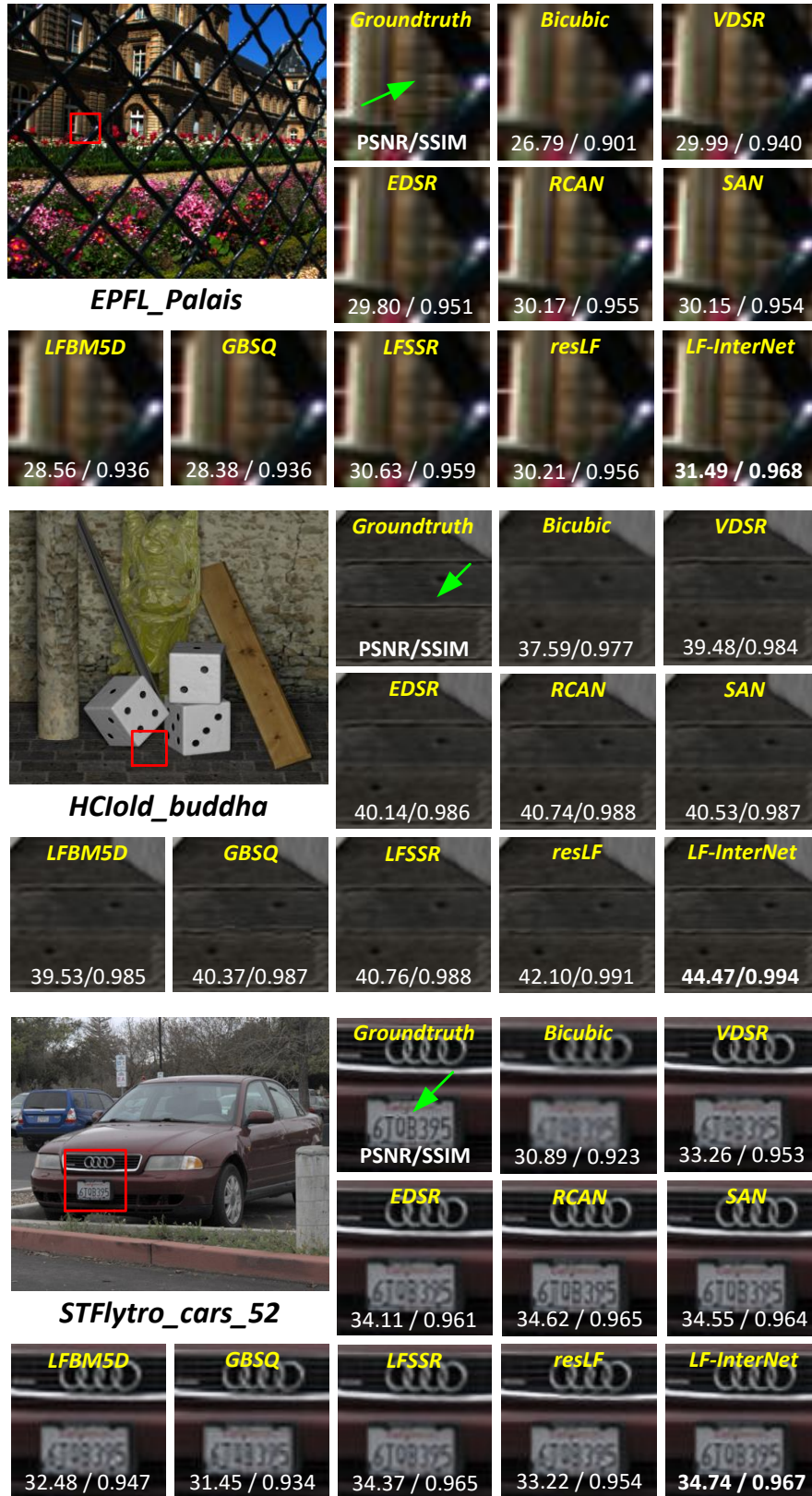


Figure 10. Additional visual results for 2×SR.

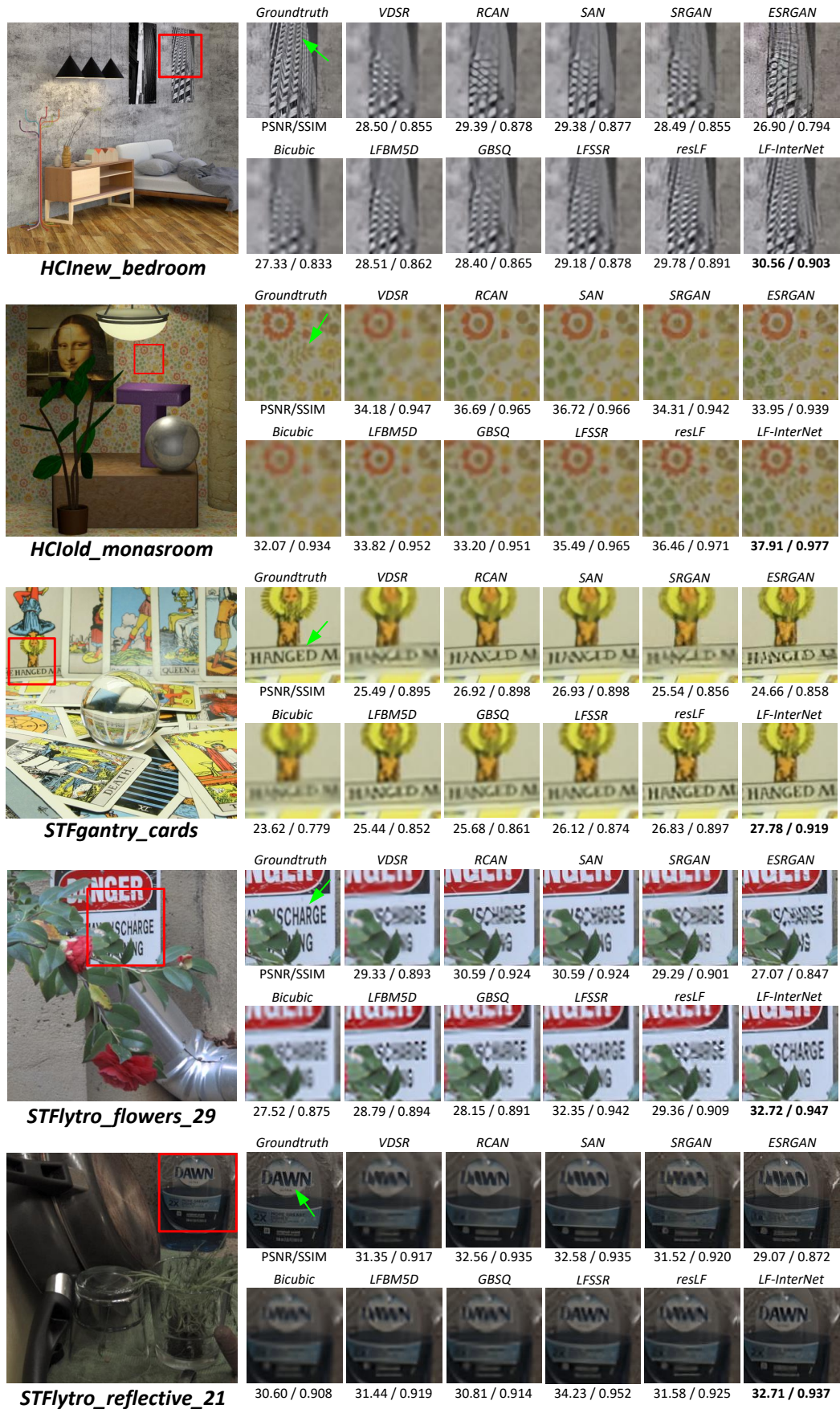


Figure 11. Additional visual results for $4\times$ SR.